Author: Ariotti, Silvia
Title: Function and behavior of CD8+ T cells in the skin
Issue Date: 2014-10-02

-2-

SUBTLE, CXCR3-DEPENDENT, CHEMOTAXIS OF CYTOTOXIC T CELLS WITHIN INFECTED TISSUE ALLOWS EFFICIENT TARGET LOCALIZATION

Manuscript under revision – Journal of Experimental Medicine

Silvia Ariotti[1,4], Joost B. Beltman[1,2,4], Rianne Borsje[1], Mirjam E. Hoekstra[1], William P. Halford[3],
John B. Haanen[1], Rob J. de Boer[2], and Ton N. Schumacher[1]

[4] These authors contributed equally to this work

[1] Division of Immunology, The Netherlands Cancer Institute, 1066 CX, Amsterdam, The Netherlands
[2] Theoretical Biology and Bioinformatics, Utrecht University, 3584 CH, Utrecht, The Netherlands
[3] Department of Medical Microbiology, Immunology and Cell Biology, Southern Illinois University School of Medicine, Springfield, IL 62794-9626, USA

It is well established how effector T cells exit the vasculature to enter the peripheral tissues in which an infection is ongoing. However, little is known on how T cells migrate to clusters of infected cells following their entry into peripheral organs. Here, we describe and analyze the migration of cytotoxic T lymphocytes (CTLs) within HSV-1 infected epidermis in vivo and demonstrate that activated T cells display a subtle CXCR3-mediated and distance-dependent chemotaxis towards clusters of infected cells. Although this chemotactic migration is weak, computer simulations based on short-term experimental data, combined with subsequent long-term imaging indicate that this behavior is crucial for efficient target localization and T cell accumulation at effector sites. Thus, chemotactic migration of effector T cells within peripheral tissue forms an important factor in the speed with which T cells are able to arrive at sites of infection.

INTRODUCTION

A striking characteristic of the cells of the immune system is their ability to travel throughout the organism to guard peripheral tissues and prevent spreading of infections. First, antigen presenting cells (APCs) acquire antigen within peripheral tissues and travel to draining lymph nodes in order to present the collected antigens to naïve T cells (Alvarez et al., 2008;Heath and Carbone, 2009). Antigen-specific T cells that are activated by APC encounter subsequently initiate expression of effector molecules such as perforin and granzymes, and enter the blood stream via the efferent lymph. Extravasation of such activated T cells preferentially takes place at sites of infection, through regulation of adhesive interactions with the vascular endothelium (Rose et al., 2007). Recent studies have examined the interaction between CTLs and target cells at sites of infection (Filipe-Santos et al., 2009;Schaeffer et al., 2009;Wilson et al., 2009). What has remained unclear however, is how T cells that have newly entered the peripheral tissue first locate these infected cells. Localization of micro-clusters of infected cells by tissue-infiltrating T cells could occur through a random migration process in which CTLs traverse the peripheral tissue without a directional preference. Alternatively, CTLs could migrate directionally towards sites of infection, a process that might increase the speed with which established sites are reached. A large number of studies have described the migration patterns of T and B lymphocytes within lymph nodes (reviewed in (Germain et al., 2012) and evidence for directed migration has been obtained in several of them (Beltman et al., 2011;Castellino et al., 2006;Hugues et al., 2007;Okada et al., 2005;Semmling et al., 2010). Within peripheral tissues (i.e., subsequent to extravasation), it was recently proposed that the observed CD8$^+$ T cell clustering around malaria-infected hepatocytes is consistent with directional migration (Cockburn et al., 2013), but direct evidence for such chemotaxis was not obtained. Other recent literature in fact suggests that CTLs in pancreas and brain adopt random search strategies (Coppieters et al., 2012;Harris et al., 2012).

Here, we develop and utilize a skin infection intravital imaging set-up in which the epidermis of recipient animals is infected with type 1 herpesvirus (HSV-1). Imaging of virus-specific and bystander CTLs within the epidermis of infected mice indicates that both T cell populations migrate through the epidermis without any directional preference that can be appreciated by direct observation. Importantly though, quantitative analysis of the data and subsequent computer simulations based on these experimental data demonstrate that there is a small, CXCR3-dependent preference to migrate towards sites of infection. Furthermore, this preference translates to a marked increase in the efficiency with which effector T cells accumulate at the sites of infection. Thus, our results reveal how subtle directed migration of cytotoxic T cells within the periphery allows the efficient localization of clusters of pathogen-infected cells during an antiviral immune response.

RESULTS

Imaging effector T cell migration in the skin

In order to detect HSV-1 infected cells within an otherwise normal tissue *in vivo*, we generated HSV-1 recombinant viruses that either express the td-tomato fluorescent protein alone (HSV$_{\text{TOM}}$), or in combination with the Ova$_{257-264}$ CD8^{+} T cell epitope (HSV$_{\text{TOM-OVA}}$). When C57Bl/6 mice were locally infected in the skin with either recombinant HSV-1 strain, multiple small foci composed of dozens of infected keratinocytes could be detected in the skin by immunohistochemistry and intravital imaging within 24 hours post-infection (Fig. 1A-B). Consistent with prior data (Weeks et al., 2000), infected microlesions were confined to the epidermal layer (Fig. 1A). Over a period of 3-4 days, these HSV-induced lesions fused together to form vesicles (Fig. S1A) that were also noticeable by visual inspection (Fig. 1C).

Control of HSV-1 infection depends on T cell immunity, as shown by the fact that infection of T cell deficient mice is lethal (Halford et al., 2004). To determine whether CD8^{+} T cells also have a role in control of infection in our recombinant HSV model, we transferred GFP-transgenic gBT I.1 TCR transgenic T cells and boosted their numbers by vaccination before infection with HSV$_{\text{TOM}}$ (Fig. S1B). Importantly, skin viral titers in HSV$_{\text{TOM}}$ infected mice harboring vaccine-activated GFP-gBT cells were markedly reduced as compared to recipients of GFP-gBT cells that had been mock vaccinated or recipients of vaccine-activated GFP-OTI T cells ($p<0.001$ in both cases, Fig. 1D). T cell control of epithelial HSV infection was also apparent by macroscopic appearance (Fig. 1C).

Analysis of viral titers at different time points post-infection demonstrated that HSV-1 specific effector T cells displayed the most pronounced effect on HSV infection between 24 and 48 hours of virus exposure (Fig. 1C), and subsequent imaging was performed at 24 hours post infection, before the occurrence of blisters and scabs that impede intravital imaging.

Imaging of HSV$_{\text{TOM}}$ infected skin demonstrated that effector T cell infiltration occurred for both HSV-specific and bystander (OTI) T cells (Fig. 2A-B; Videos S1-S3). To subsequently visualize the movement of effector T cells within the epidermis, infected skin-areas infiltrated with GFP^{+}CD8^{+} T cells were imaged at one-minute intervals for up to one hour (without measurable phototoxicity; Fig. S2). Whereas both gBT and OTI T cells actively moved around HSV$_{\text{TOM}}$ infected microlesions (Videos S1-S3), only gBT cells arrested in close proximity to sites of infection, as demonstrated by decreased speed and loss of persistent migration (Fig. 2C-D; Fig. S3A-B for 3D analysis). This T cell arrest was due to antigen recognition (Boissonnas et al., 2007), as OTI T cells in the skin of mice infected with HSV$_{\text{TOM-OVA}}$ also decreased their speeds close to the site of infection (Fig. 2C-D; Fig. S3).

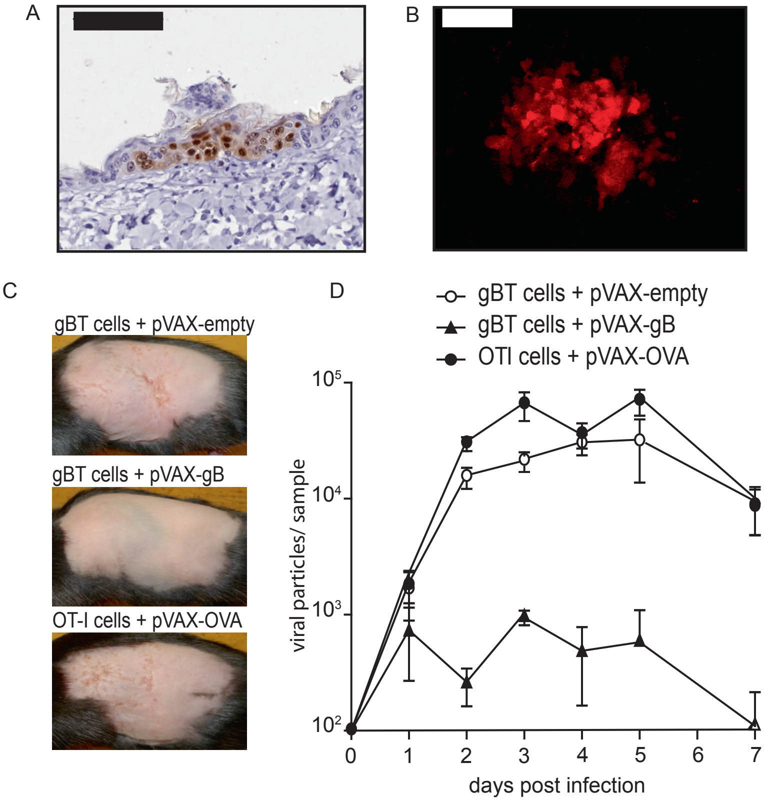

Figure 1. Characterization of intraepithelial HSV-1 infection.
(A) Left: Transverse section of paraffin-embedded skin stained with anti-HSV antibody (brown), 24 hours after intraepithelial infection with HSV_{TOM}. Bar = 100 µm. **(B)** Confocal (top view) image of an HSV-1 infected area (red), 24 hours after intraepithelial infection with HSV_{TOM}. Bar = 100 µm. **(C, D)** Recipients of naïve GFP-gBT or GFP-OTI T cells were vaccinated with DNA encoding the indicated epitope or with empty vector. Ten days later, the flank skin was intraepithelially infected with HSV_{TOM}. **(C)** Fotographs of mice in the different experimental conditions at day 7 post infection. **(D)** On the indicated days after infection, mice (n=3 per group, representative of two experiments) were sacrificed and viral titers in HSV-infected skin were determined by Q-PCR. Data are represented as mean +/- SEM.

Subtle directed migration of skin effector CD8⁺ T cells

In order to determine by which migration strategy effector T cells reach foci of infection after tissue entry, we quantified the angle to infection (i.e., the angle between the measured travel direction and the shortest route towards the infection) for each movement step. Average angles to infection were then plotted as a function of distance to the infection to detect a possible preferential migration direction (Beltman et al., 2009). Analysis of T cells around infected lesions showed a small but clear distance-dependent deviation from 90 degrees in the average angle of infection (Fig. 2E; Fig. S3C). Specifically, at the vicinity of the infection (0-25 µm), angles to infection were not significantly different from 90 degrees (gBT+HSV$_{\text{TOM}}$: p=0.51; OTI+HSV$_{\text{TOM}}$: p=0.32; OTI+HSV$_{\text{TOM-OVA}}$: p=0.59; Mann-Whitney test), implying random migration. In contrast, migration angles of T cells located further away from the infection (more than 25µm) were significantly smaller than 90 degrees (gBT+HSV$_{\text{TOM}}$: p=0.003; OTI+HSV$_{\text{TOM}}$: p<0.001; OTI+HSV$_{\text{TOM-OVA}}$: p=0.003; Mann-Whitney test). Thus, while T cells around HSV-infected lesions do migrate in all directions, a small but highly significant preference for directions that bring the cell closer to the site of infection is observed. This distance-dependent preferential migration was similar for ag-specific and bystander T cells (Fig. 2E and S3C; differences between mean angles to infection were non-significant for all comparisons; Mann-Whitney test). Thus, the attracting component in T cell migration is independent of cognate antigen. Finally, when T cell migration was analyzed as the average displacement rate of cells towards the infection as a function of distance from infection (Fig. 2F and S3D), a distance-dependent pattern of attraction towards the site of infection was observed for all three conditions tested. Specifically, whereas close to the infection (up to 25 µm away) displacement rates towards infection were not different from 0 µm/min (gBT+HSV$_{\text{TOM}}$: p=0.60; OTI+HSV$_{\text{TOM}}$: p=0.42; OTI+HSV$_{\text{TOM-OVA}}$: p=0.57; Mann-Whitney test), further away from the infection (more than 25 µm away) an average displacement rate of 0.3-0.4 µm/min -significantly different from zero (gBT+HSV$_{\text{TOM}}$: p=0.002; OTI+HSV$_{\text{TOM}}$: p<0.001; OTI+HSV$_{\text{TOM-OVA}}$: p=0.027; Mann-Whitney test)- was observed. In summary, effector T cells in the epidermis migrate in all directions, but with a small, antigen-independent preference for movement towards infected areas. Comparison of individual videos also revealed that the attraction of effector T cells is positively correlated to the size of the microlesions (Supplementary text; Fig. S4).

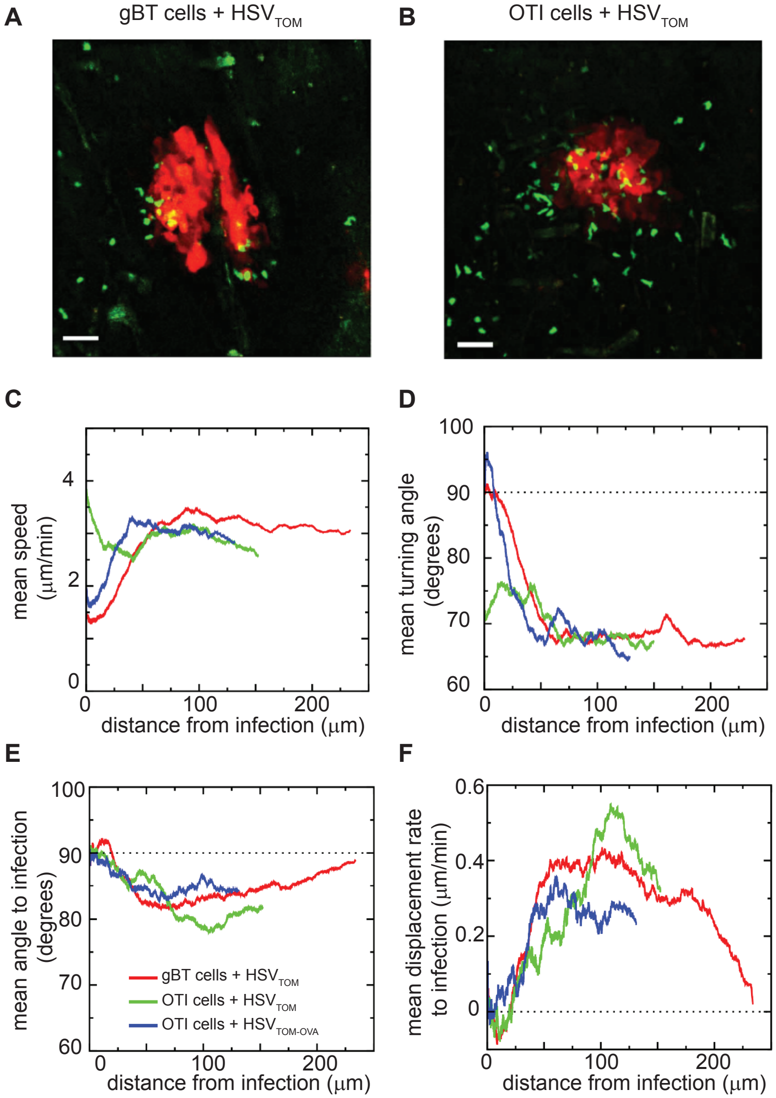

Figure 2. CTLs migrate preferentially towards infected microlesions.
(A, B) Still confocal images of effector T cells (green) and HSV-1 infected microlesions (red) in epidermal skin of recipients of GFP-gBT (A) and GFP-OTI (B) $CD8^+$ T cells. Bar = 50µm. **(C to F)** The mean speed (C), mean turning angle (D), mean angle to infection (E) and mean displacement rate towards infection (F) of skin-infiltrating effector T cells are depicted as a function of the mean distance to the border of the infection. All tracked movement steps were sorted according to distance from infection (after merging data from multiple experiments), and a running average of 2,000 data points was plotted (note that for each 'bin' the mean value is calculated for both axes). Colors represent the following groups: GFP-gBT T cells (4 videos from 4 mice) and GFP-OTI T cells in animals infected with HSV_{TOM}, (5 videos from 5 mice; red and green, respectively), and GFP-OTI T cells in animals infected with $\text{HSV}_{\text{TOM-OVA}}$ (4 videos from 4 mice; blue). Analyses in 3D are provided in Fig. S3.

Modeling the consequence of directed migration of effector T cells

The observed directional preference of CTLs towards sites of infection is relatively small (Fig. 2E), and the variation among all measured angles to infection is very large (lower panels of Fig. S5), thereby explaining why directional migration is not apparent from visual inspection of in vivo imaging data (videos S1-S3). To determine to what extent T cell arrival at sites of infection is influenced by this small directional preference, we generated realistic, long-lasting tracks based on experimental data by a computational approach similar to previously published work (Beauchemin et al., 2007;Figge et al., 2008;Beltman et al., 2011). We reconstructed cellular migration paths using the experimentally measured distributions of speed, angle to infection and turning angle. Furthermore, because the distance to infection at which cells are located determines the typical values found for these three parameters, we chose combinations of speed and migration angles from data points that were binned with respect to their distance from the infection.

During each simulation, *in silico* CTLs started at a predefined distance away from the circular (or spherical) infection, and combinations of speed and migration angles were drawn at random from the experimental distributions found around that distance. The resulting migration step determined the position, and therefore the distance to the infection, of the next time step. This procedure was repeated until a cell arrived in proximity of the infection, or left the space for which we had experimental data (i.e., reached distances too far away from the infection). The tracks generated (e.g., Fig. 3A) matched the experimental data closely in terms of their distributions of speed, angles to infection and turning angles (Fig. S5). In addition to these 'directed' simulations, we also performed 'random' simulations in which we substituted the experimentally found distribution of angles to infection with a random distribution, while keeping the persistence and speed of cells according to the experimental measurements (Fig. 3B).

Both specific and bystander cells starting at a distance of up to around 150 μm arrived with almost 100% efficiency close to the infection when directed simulations were performed (Fig. 3C). In contrast, for randomly moving cells, regardless of their specificity, the fraction of cells that reached the target was only around 30%. Furthermore, the cells that did arrive at the infection by random migration required approximately twice the amount of time as directional cells (Fig. 3D). The differences between directed and random simulations were observed both when simulations were performed in 2D (Fig. 3), and when performed in one-side-restricted or two-side-restricted 3D (Fig. S6). As a side note, the approach speed of *in silico* OTI cells towards HSV$_{\text{TOM-OVA}}$ lesions is lower than towards HSV$_{\text{TOM}}$ lesions (Fig. S6) and the measured attraction in the *in vivo* data also appears slightly lower (Fig. 2E-F, non-significant), an observation possibly explained by a lower growth rate of HSV$_{\text{TOM-OVA}}$ infection foci, thereby lowering attraction strength (see Supplementary Text and Fig. S4).

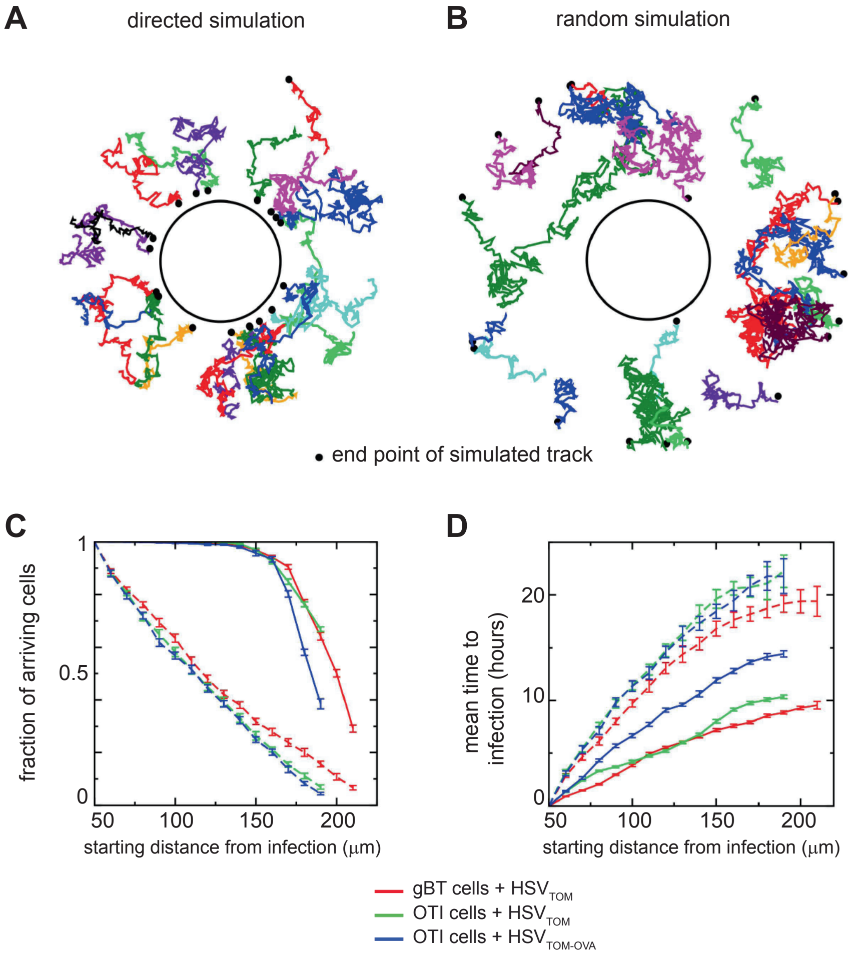

Figure 3. Simulating the effect of directional migration on T cell arrival.
(A and B) Example of tracks of 20 *in silico* gBT T cells starting at a 150 µm distance from an infection with radius r=100µm, constructed by 'directed' (A) or 'random' (B) 2D simulations. The black circle indicates the perimeter of the simulated infection, and the black dots represent the final position of cells. **(C and D)** The fraction of cells arriving at a 50 µm distance from an infection with radius *r*=100µm (C) and the mean time to achieve this (D), when starting from various distances to infection in 2D simulations. For each starting distance to infection, 20 simulations of 1,000 cells were performed; mean and standard deviations of the simulations are plotted. Results from directed simulations are shown by solid lines, results from random simulations by dashed lines. Simulations are based on cell migration data from GFP-gBT T cells and GFP-OTI T cells in animals infected with HSV_{TOM}, (red and green, respectively), and of GFP-OTI T cells in animals infected with $HSV_{TOM\text{-}OVA}$ (blue). Migration data from gBT cells at distances to infection higher than about 210 µm were omitted from the analysis in order to allow for a fair comparison between experimental conditions.

Long-term in vivo imaging confirms predicted CTL accumulation

In the above experiments, we used short-term imaging data to generate simulations that showed the long-term consequences of the observed bias in angles to infection (Fig. 3 and S6). These simulations rely on two essential assumptions: first, that the T cell migration parameters observed during imaging at 24 hours post infection hold true for longer periods; second, that the T cell migration parameters measured are the major factors in driving T cell accumulation, rather than T cell division or death/ exit. In order to test whether *in vivo* T cell accumulation followed the pattern predicted by our simulations, we performed 'long-term – long-interval' *in vivo* imaging experiments (lasting up to 12 hours), monitoring both the spatial distribution of gBT T cells and infection growth (Fig. S7A). Analysis of the still images showed a clear accumulation of T cells close to the infection over time (Fig. 4A-B).

We then simulated CTL migration towards the infection, using the distance distribution observed at the first still time point of imaging (time ≈17 hours) as a starting distribution; in addition, we simulated new cells entering the simulated field at a random position in space and time, such that the same amount of cells was present at the final time point in our simulations as in the imaging data set; finally, we took into account the infection growth observed during imaging. The spatial distributions at the end of the directed simulations (up to 12 hours) matched the experimentally observed spatial distributions very well (Fig. 4C and S7B). In contrast, the match between the spatial distribution observed in random simulations and that observed *in vivo* was poor. On the basis of these data, we conclude that the accumulation that is observed *in vivo* does require directional migration, and cannot be explained by random migration combined with arrest close to the infection.

To explore the same issue for T cells that do not encounter cognate antigen, we subsequently performed the same imaging and simulation procedure for OTI bystander cells, which continue migrating when entering the lesion. In this case, directed migration alone consistently overpredicted the accumulation of effector cells close to the infection (Fig. S8). Extension of the simulations with a probability to leave the infiltrated area after arrival at the infected site (e.g. by exit of the imaging field towards the dermis) improved the correspondence between predicted and observed spatial distribution. This suggests that T cells that fail to detect cognate antigen may have an increased probability to leave the infiltrated area after a period of unfruitful search.

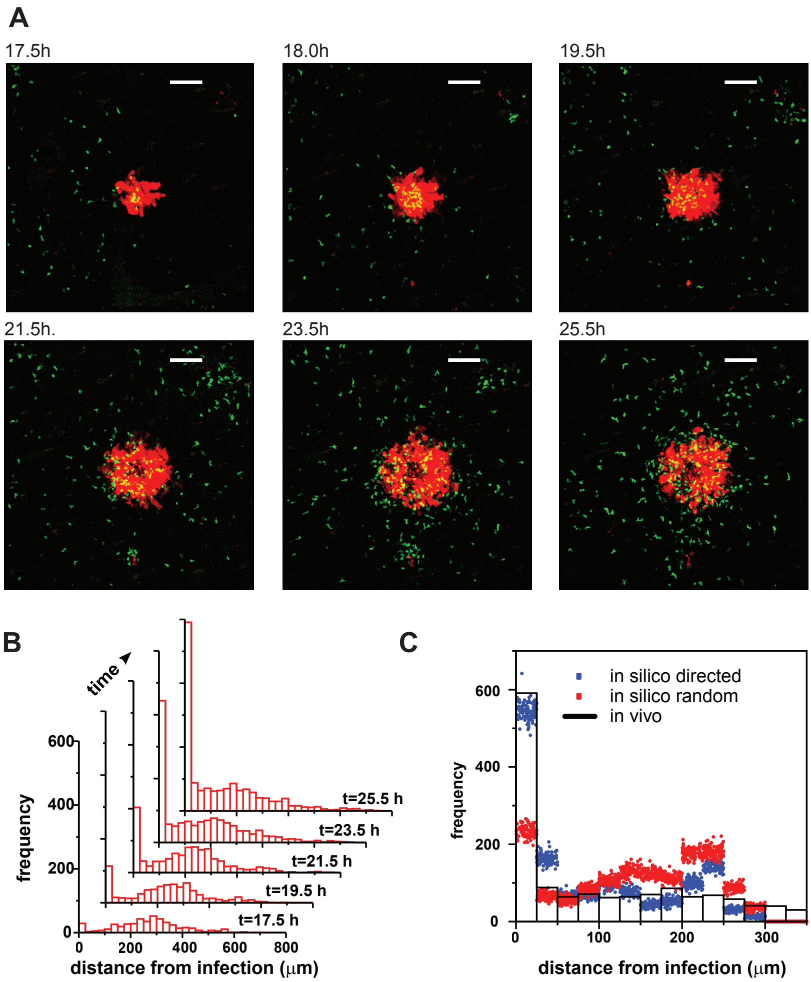

Figure 4. CTLs accumulate around infected microlesions over time.
(A) Still confocal images of GFP-gBT T cells (green) and microlesions (red) in epidermal skin, showing accumulation of T cells close to the infection over time. Bar = 100μm. **(B)** Evolution of the distance distribution of effector T cells over time. Data of consecutive image sequences obtained from eight different infected areas within a single mouse (representative of three mice) were combined. **(C)** Comparison of the experimental spatial distributions of gBT cells and the distributions of gBT cells from simulations in which migration was either directed or random (in 2D), in the context of a growing infection. *In silico* cells were simulated considering a combination of: (1) the initially observed spatial distribution taken from experimental data at approximately 17 hours after infection, (2) the entry of new cells in the epidermis at random time points and at random locations in the simulated space, (3) an initial infection radius as estimated from the images, and a growth of the infection radius at a rate determined from the experimental images (about 0.1 μm per minute). Bars represent the experimental distribution at the last time point of imaging, dots represent the simulated distributions. Results for two other mice are presented in Fig. S7B. Note that the simulations exhibit a peak in cell number around 200 μm from infection. This is due to a transition to random migration and possibly attraction towards a neighboring infection focus at very large distances, which in the simulation leads to cells lingering around at distances of approximately 200 μm.

CXCR3 mediates chemotaxis of effector T cells in the skin

Finally, we wanted to investigate which signals mediate the directional migration of effector T cells within the skin. To this purpose, we transferred GFP-OTI-$CXCR3^{-/-}$ cells ($CXCR3^{-/-}$ cells; Fig. 5A) into C57Bl/6 mice, which were then vaccinated with SIINFEKL and infected with HSV_{TOM}. Following HSV_{TOM} administration, effector T cells from $CXCR3^{-/-}$ donor origin were found at the site of infection, albeit at slightly lower frequencies than wild type cells. Importantly, the $CXCR3^{-/-}$ T cells infiltrating the area of infection did not exhibit the strong accumulation around sites of infection seen for wild type OTI T cells (Fig.5B-C). Furthermore, whereas control T cells showed directed migration at long distances from the infection, no significant directional migration could be detected for CXCR3 deficient T cells (Fig.5D-E). The small (non-significant) directed migration component that might still be present, especially for distances more than 200 µm from infection (data not shown) could suggest that other chemokine receptors may also have a limited role in attracting T cells towards infection foci. However, signaling via CXCR3 clearly explains the bulk of the directional migration observed.

As an independent test for the involvement of CXCR3 that does not rely on genetic deficiency of the receptor, we explored the effect of local delivery of CXCL10. When the pre-existing chemokine gradient was disrupted by local delivery of CXCL10 by tattoo application, the consistent pattern of T cell migration towards foci of infection was no longer observed. Specifically, T cells around individual foci either revealed migration away from or towards foci, or migration in an approximately random pattern, consistent with the notion that T cells were attracted to newly created CXCL10 hotspots (Fig. S9). Taken together, these data show that the directed migration displayed by CTLs in proximity of foci of infection is largely mediated by CXCR3 and its ligands.

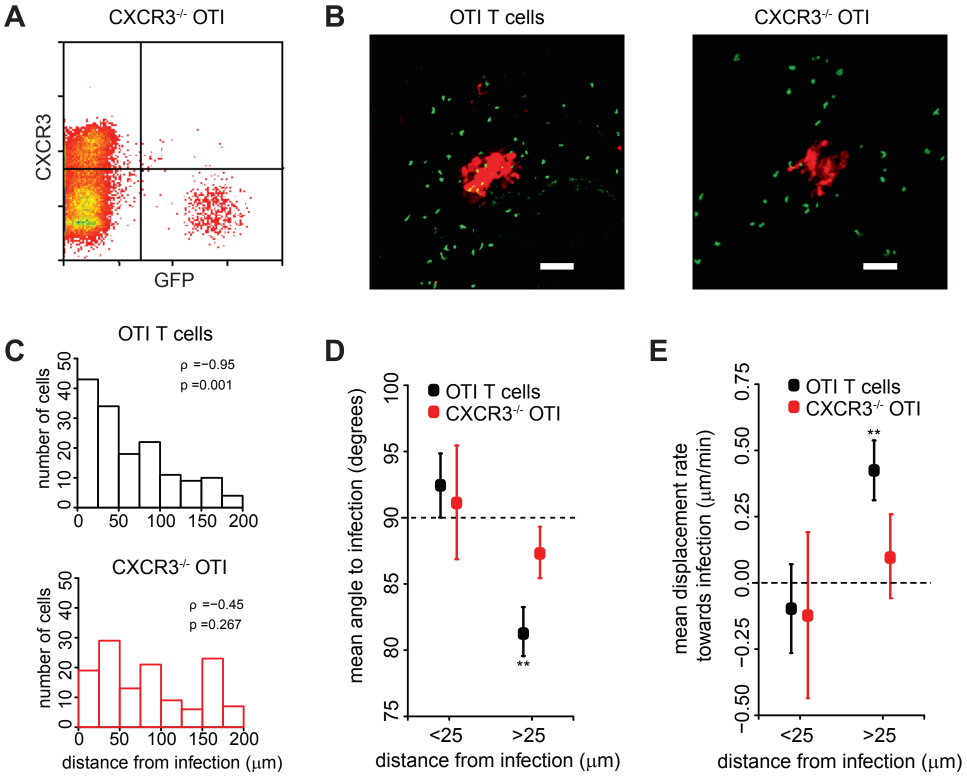

Figure 5. Directed migration of CTLs is CXCR3 dependent.
(A) Recipients of naïve GFP-OTI-CXCR3$^{-/-}$ T cells were vaccinated with DNA encoding the SIINFEKL epitope to activate the adoptively transferred cells. **(B)** Still confocal images of GFP-OTI or GFP-OTI-CXCR3$^{-/-}$ T cells (green) and HSV$_{TOM}$ microlesions (red) in epidermal skin. Bar = 100µm. **(C)** Comparison of the experimental spatial distributions of GFP-OTI or GFP-OTI-CXCR3$^{-/-}$ T cells (pooled from five imaging regions from 5 and 2 mice, respectively) at 24 hours post HSV$_{TOM}$ infection. **(D-E)** The mean angle to infection (D) and displacement rate towards infection (E) for GFP-OTI or GFP-OTI-CXCR3$^{-/-}$ T cells close (<25 µm) or far (>25 µm) from the infection. Wild type OTI T cells far away from the infection displayed migration parameters that differed significantly from the values expected for random migration (denoted by dashed lines; ** p<0.005); the migration pattern of GFP-OTI-CXCR3$^{-/-}$ T cells is, on the contrary, consistent with random migration.

DISCUSSION

The main finding of the current study is that effector $CD8^+$ T cells in skin epithelium approach clusters of infected cells by subtle chemotaxis. This directed migration can be described as a small preference for movements towards the microlesion in an otherwise highly irregular trajectory, and in fact the T cells move away from the sites of infection almost as often as they move towards it.

The observed CXCR3-mediated attraction of T cells by clusters of infected cells implies the existence of a chemoattractant gradient, and the finding that the strength of T cell attraction correlates with lesion size is also consistent with this notion. If T cells are guided to sites of infection by a gradient, why is their migration pattern so erratic? One explanation is that T cell migration has to occur through a bed of tightly linked keratinocytes, thereby severely limiting the number of potential trajectories. This, however, does not seem to explain why T cells also frequently move away from the site of infection. Conceivably, the gradient that is sensed by the cells is locally stochastic and shallow. A shallow chemotactic gradient may make it difficult for small cells such as T lymphocytes to respond to the signal due to the minimal difference in signal strength sensed by the front and back end of the cell (Bialek and Setayeshgar, 2005). However, neutrophils have a similar size as T cells and seem to be able to migrate directionally in a much more pronounced manner, both intravascularly and within peripheral tissues (McDonald et al., 2010;Peters et al., 2008;Lammermann et al., 2013). Thus, it might also be a general property of T cells that random and persistent trajectories are adjusted only slightly upon encounter of chemoattractant gradients, possibly to allow the scanning of a larger area of the peripheral tissue.

Upon HSV infection, both specific and bystander effector T cells are found within the infected area (Fig. 2A), consistent with prior data from other groups on the behavior of effector T cells in tumors and infected tissues (Boissonnas et al., 2007;Koya et al., 2010;Mrass et al., 2006). The presence of substantial numbers of non-specific T cells could reduce the efficiency of cognate CTL-target cell contacts by steric hindrance. For the similar case of T cell scanning of dendritic cells within lymph nodes, we recently demonstrated that such competition can be alleviated if bystander T cells loose their sensitivity to chemokine upon reaching the APC (Vroomans et al., 2012). By the same token, in the case of skin infection, this 'logistic' problem could be reduced when effector T cells that do not encounter their cognate antigen were to leave the infected area, a concept that is supported by our *in silico* simulations of bystander cells.

Two observations suggest that the chemoattraction that we describe here is biologically meaningful. First, the pattern of T cell accumulation that is measured experimentally is reproduced in computer simulations in which the observed directional migration is incorporated, but not in simulations in which accumulation is driven by a combination of random T cell migration and T cell arrest close to the infection. Second, the observed chemotaxis influences T cell arrival on a time scale that is relevant to the kinetics of HSV-1 spreading within the infected skin (according to our *in vivo* measurements by a radial growth of approximately three cell layers, in five hours). To our knowledge, this study presents the first direct evidence of chemoattraction towards regions of interest of effector T cells within a peripheral tissue. Prior studies in other peripheral tissues did not detect directional migration (Coppieters et al., 2012;Harris et al., 2012), or postulated its occurrence on the basis of indirect observations (Cockburn et al., 2013). It may be interesting to re-analyze such existing data by the strategies used here, in order to evaluate whether similar subtle migration behaviors are 'hidden' in time-lapse imaging data sets.

MATERIALS AND METHODS

Mice

C57Bl/6, C57Bl/6 actin-GFP and C57Bl/6 OT-I TCR transgenic mice were obtained from Charles River Laboratories and housed in the animal department of the Netherlands Cancer Institute (NKI). C57Bl/6 gBT TCR transgenic mice (Mueller et al., 2002) were a kind gift from Dr. F. Carbone (University of Melbourne, Australia). All animal experiments were approved by the Experimental Animal Committee of the NKI, in accordance with national guidelines.

Reagents

Antibodies against MHC II, CD4, CD11b, CD11c, Ter-119, CD49b, CD45R, Gr-1 and CD8 were obtained from BD Biosciences. MHC-tetramers loaded with SIINFEKL ($Ova_{257–264}$) or SSIEFARL ($gB_{498–505}$) peptides were produced by UV-induced ligand exchange (Toebes et al., 2006) and labeled with PE or APC (Invitrogen).

DNA vaccines were generated by the introduction of the indicated fusion genes in pVAX. Tetanus Toxin Fragment C (TTFC)-Ova and TTFC-gB DNA sequences were designed for optimized codon usage, and encoded domain I of TTFC and the indicated T cell epitope, separated by a GVQI peptide linker. HSV_{TOM} and $HSV_{TOM\text{-}OVA}$ viruses were constructed by the insertion of a CMV immediate-early promoter-tomato (or tomato-$Ova_{257–264}$) gene cassette into the intergenic region between the UL26 and UL27 genes of the HSV-1 strain KOS, as described previously (Halford et al., 2004).

Flow cytometry

For the measurement of T cell responses, 25 µl of peripheral blood was collected in heparin-coated vials (Microvette, Omnilabo) at the indicated days post transfer. Following removal of erythrocytes by NH_4Cl treatment, cells were stained with the indicated Abs and analyzed by flow cytometry. Dead cells were excluded by DAPI staining. Cell sorting was performed on a FACSAria cell sorter using FACSDiva software (v5.0.1; both from BD), or a MoFlo high-speed sorter using Summit software (v3.1; both from Beckman Coulter). Analyses were performed on a CyAn$_{ADP}$ using Summit software (v4.3; both from Beckman Coulter).

Adoptive transfer and intradermal DNA vaccination

Spleens from GFP-gBT or GFP-OT-I mice were isolated and homogenized by mincing through cell strainers (BD Falcon). After red blood cell lysis, CD8$^+$ T cells were isolated, using MHC II$^+$, CD4$^+$, CD11b$^+$, CD11c$^+$, Ter-119$^+$, CD49b$^+$, CD45R$^+$ and Gr-1$^+$ staining as exclusion criteria. C57Bl/6 mice were injected intravenously with 2.0x10^5 sorted naïve CD8$^+$ T cells. Intradermal DNA vaccination with either TTFC-Ova or TTFC-gB was carried out on the shaved hind leg of anesthetized mice, as described in (Bins et al., 2005). In brief, a droplet of 30µg of DNA in 15µl of PBS was applied onto the skin and injected using a sterile disposable 11-needle bar mounted on a rotary tattoo device. Needle depth was adjusted to 0.5mm and the needle bar oscillated at 100Hz for a 60s tattoo.

HSV-1 infection, Quantitative PCR and Immunohistochemistry

Indicated HSV strains were grown in Vero cells as described (Halford et al., 2004) and intraepithelial HSV-1 infection was carried out on the shaved flank of anesthetized mice. In brief, a droplet of 20 µl of virus-infected Vero cell supernatant containing approximately 2.5x10^5 pfu was applied onto the skin and introduced as described for intradermal vaccination, but with needle depth adjusted to 0.05mm, for a 20s tattoo. At the indicated time points post infection, mice were sacrificed; the skin of the infected flank was collected and divided into two separate specimens that were further treated independently. HSV titers (Artus HSV-1/2 TM PCR Kit, Qiagen) were analyzed in triplicate on each half sample, according to protocol. HSV infection was visualized by incubation with rabbit polyclonal anti HSV antibody (Thermo Scientific) followed by PowerVision Poly-HRP-Goat anti Rabbit staining (ImmunoLogic) and DAB reaction (Dako Cytomation), according to protocol.

Confocal Microscopy and Image Analysis

Twenty-four hours after HSV infection, mice were anesthetized using a mixture of air and isoflurane (Baxter) and placed in a custom-built chamber with the infected flank gently placed against a coverslip at the bottom side of the chamber. Images were acquired using an inverted Leica TCS SP2 confocal scanning microscope (Leica microsystem) equipped with Diode and Argon lasers and enclosed in a custom-built environmental chamber that was maintained at 37°C using heated air. Images were acquired using a 20×/0.7 NA dry objective unless indicated otherwise. GFP was excited at 488nm wavelength and tomato at 561nm. Typical voxel dimensions were 0.9-2.0 µm laterally × 1.5–2.5 µm axially. Three-dimensional stacks (typical size: ~500µm x ~500 µm x ~30µm) were captured every minute for a period of up to 2 hours. Raw imaging data were processed with Imaris (Bitplane). Imaris Spots module was used to track objects and to calculate cell coordinates (mean positions) over time (representative track in Video S4).

Cell migration analysis

The cell coordinate data that resulted from tracking were corrected for artifacts as described in (Beltman et al., 2009). In brief, (auto-) fluorescent objects that appeared static were used for approximate tissue drift correction. Movement steps close to the borders of the image volume were discarded from analysis because they would appear to move parallel to those borders due to tracking errors (note that an advantage of 2D over 3D analyses is that a much smaller number of movement steps need to be discarded for this reason). Finally, imprecision in the axial resolution was corrected by multiplying the mean axial speed of cells by a factor (varying between 1.2 and 2.95 depending on the experiment) that made it approximately equal to their mean lateral speed. Because of the flat structure of the epidermis, it is possible that axial speeds are in fact much smaller than lateral speeds. Omitting the axial speed correction would entail that the lateral movements are much more important than the axial movements in determining arrival at microlesions, i.e., that migration is effectively two-dimensional. Indeed, the observed directional preference of CTLs towards infected microlesions was observed both with and without the correction for axial speed (data not shown).

After correction for these artifacts, the following parameters were calculated from the cell coordinates: (1) cell speeds (during individual movement steps); (2) turning angles (i.e., the angle between subsequent movement steps of a cell); (3) distances to infection (i.e., distance between the center of mass of a cell and the location of the most nearby voxel that was assigned to the infection when using a segmentation threshold following application of a Gaussian filter to smoothen the images); (4) angles to infection (i.e., the angle between the direction of migration of a cell and the direction towards the nearest voxel assigned to the infection); and (5) displacement rates towards infection (calculated from the projection of a movement step onto the vector that represents the shortest route towards the nearest voxel assigned to the infection). Note that all the studied migration parameters are averages measured over 1-minute time frames.

Model of cell migration

Cell motion was modeled by describing it as a series of discrete steps in space. Simulations were performed in two or three dimensions, and as ‘directed’ or ‘random’ simulations. For directed simulations, the experimental distributions of speed, angle to infection and turning angle were used after merging the data from four to five experiments that were performed under the same conditions. Measured pairs of speed and angle to infection were maintained during directional simulations. In random simulations, the angles to infection were chosen from a distribution as expected for random migration, i.e., a uniform distribution in 2D and a sine distribution in 3D. The distributions of speed and angle to infection were sorted according to the distance to infection at which the measurement was taken. Subsequently, the speed/angle-to-infection pairs were binned into distance categories containing 100 measurements each. Each of the distance bins would also be accompanied by a turning angle distribution (containing all the turning angles experimentally measured in that distance bin). In the simulations, a microlesion was modeled as a circle (in 2D) or sphere (in 3D) with radius *r*. Each *in silico* cell was initialized at the indicated distance from the simulated infection, and the initial movement step of the cell was chosen at random from the 100 speed/angle-to-infection combinations in the appropriate distance category. In 2D simulations, each combination is associated with two possible movement steps and one of them would be chosen at random. In 3D simulations, the possible movement steps for each combination can be described by a circle in 3D space, and a random position on that circle was chosen. The cell was then moved to the new position defined by the chosen step. Subsequent movement steps were again chosen from the allowed speed/angle-to-infection pairs. However, if the movement steps were to be chosen randomly from the pairs, a turning angle distribution without any persistence would ensue. In particular, this would lead to a turning angle distribution close to a uniform distribution for 2D simulations and close to a sine distribution for 3D simulations (Beltman et al., 2009). Therefore, we built in the extra restriction that a chosen movement step was accepted with a probability that would ensure a similar turning angle distribution in the simulations as in the experimental data. To achieve that, the turning angle distribution of each distance category was discretized into 18 bins of 10 degrees wide, and the proportion p_i of each turning angle bin was recorded for all distance categories (where i represents the turning angle bin number from 0 to 18). For 2D simulations, we took the proportion of the turning angle bin in which the step under consideration would fall (p_i) as the acceptance probability for that step. For 3D simulations, the proportion of each turning angle bin was first weighted by the factor $w_i = 1/\int_{\alpha=a}^{b} \sin(\alpha)d\alpha = 1/(\cos(a) - \cos(b))$, where a and b are the lower and upper limit of a turning angle bin, e.g., for the first bin a=0 and b=10 degrees. Next, the weighted and normalized proportion $\frac{p_i w_i}{\sum_i p_i w_i}$ was used as acceptance probability for the step. This normalized weighting of proportions ensured that speed-angle-to-infection combinations were sampled in a manner that resulted in a correct turning angle distribution. When a movement step was not accepted, another movement step would be chosen at random until one was accepted.

We performed two types of 3D simulations, one in which CTL migration was restricted at the exterior side, and one in which it was in addition restricted at the interior side. These restrictions were implemented by discarding movement steps that would result in a crossing of the interior or exterior side during the sampling of movement steps.

Simulations of long-term (up to 12 hours) T cell accumulation were performed in 2D. Infection growth was described as linear, radial growth following experimental measurements of infection sizes, and directed as well as random cell migration was simulated as described above. For bystander OTI cells, we considered the possibility that T cells reaching the infection from that moment could leave the simulated region (in the axial direction, i.e., by leaving the epidermis). In these 'simulations with leaving', at each time step T cells that had earlier reached the infection, left with probability δ.

Statistical Methods

A linear mixed effects model was constructed to determine if viral load differed between treatments over the week after inoculation. Joint Wald tests were performed on linear and quadratic coefficients, and Bonferroni-adjusted significance level for the two-sided test was set at 0.017.

Because of persistent migration of T cells at short time intervals, subsequent movement steps are not independent. Therefore, statistics were applied to steps that were at least 10 minutes apart, because for skin T cells the correlation in movement direction was approximately lost after this time interval (data not shown). Two-tailed Mann-Whitney tests (using the software package R) were performed to study whether cell migration differs from a random walk, and to compare migration parameters in different conditions. Spearman's rho between distance from infection and the number of cells at that distance was calculated to study whether spatial distributions exhibited a consistent decline with distance from infection, as expected for chemoattraction towards foci of infection. A p-value below 0.05 was considered significant.

Online supplemental material

Fig. S1 shows the kinetics of HSV-1 infection spreading and immune response *in vivo*. Fig. S2 shows that phototoxicity does not affect T cell behavior in our experimental set-up. Fig. S3 shows 3D analysis of T cell migration. Fig. S4 shows the relation between infection size and T cell attraction and infiltration. Fig. S5 shows comparisons of experimental and simulated angles and speed distributions. Fig. S6 shows the effect of directed migration as tested in 3D *in silico* simulations. Fig. S7 and S8 show the accumulation of infection specific and bystander cells around infection foci. Fig. S9 shows the loss of directed migration by CTLs upon disruption of the CXCL10 gradient. Video S1 shows GFP-gBT cells infiltrating an $\mathrm{HSV}_{\mathrm{TOM}}$ infected area. Video S2 and S3 show GFP-OTI cells infiltrating an $\mathrm{HSV}_{\mathrm{TOM}}$ or $\mathrm{HSV}_{\mathrm{TOM\text{-}OVA}}$ infected area, respectively. Video S4 shows a representative T cell track.

ACKNOWLEDGEMENTS

We thank the Flow Cytometry Facility for cell sorting, the Digital Microscopy Facility and Kees Jalink for excellent technical support and advice; Ruud van Mierlo for daily assistance and Johannes Textor for discussions. This work was supported by the Netherlands Organization for Scientific Research (NWO), grants 912.10.066 (TNS and RJdB), 916.86.080 (JBB) and 016.048.603 (RJdB), and European Research Council Grant Life-his-T (TNS).

REFERENCES

1. Alvarez, D., E.H.Vollmann, and U.H.von Andrian. 2008. Mechanisms and consequences of dendritic cell migration. *Immunity* 29:325-342.
2. Beauchemin, C., N.M.Dixit, and A.S.Perelson. 2007. Characterizing T cell movement within lymph nodes in the absence of antigen. *J Immunol* 178:5505-5512.
3. Beltman, J.B., C.D.Allen, J.G.Cyster, and R.J.de Boer. 2011. B cells within germinal centers migrate preferentially from dark to light zone. *Proc Natl Acad Sci U S A* 108:8755-8760.
4. Beltman, J.B., A.F.Maree, and R.J.de Boer. 2009. Analysing immune cell migration. *Nat Rev Immunol* 9:789-798.
5. Bialek, W. and S.Setayeshgar. 2005. Physical limits to biochemical signaling. *Proc Natl Acad Sci U S A* 102:10040-10045.
6. Bins, A.D., A.Jorritsma, M.C.Wolkers, C.F.Hung, T.C.Wu, T.N.Schumacher, and J.B.Haanen. 2005. A rapid and potent DNA vaccination strategy defined by in vivo monitoring of antigen expression. *Nat Med* 11:899-904.
7. Boissonnas, A., L.Fetler, I.S.Zeelenberg, S.Hugues, and S.Amigorena. 2007. In vivo imaging of cytotoxic T cell infiltration and elimination of a solid tumor. *J Exp Med* 204:345-356.
8. Castellino, F., A.Y.Huang, G.Altan-Bonnet, S.Stoll, C.Scheinecker, and R.N.Germain. 2006. Chemokines enhance immunity by guiding naive CD8+ T cells to sites of CD4+ T cell-dendritic cell interaction. *Nature* 440:890-895.
9. Cockburn, I.A., R.Amino, R.K.Kelemen, S.C.Kuo, S.W.Tse, A.Radtke, L.Mac-Daniel, V.V.Ganusov, F.Zavala, and R.Menard. 2013. In vivo imaging of CD8+ T cell-mediated elimination of malaria liver stages. *Proc Natl Acad Sci U S A* 110:9090-9095.
10. Coppieters, K., N.Amirian, and M.von Herrath. 2012. Intravital imaging of CTLs killing islet cells in diabetic mice. *J Clin Invest* 122:119-131.
11. Figge, M.T., A.Garin, M.Gunzer, M.Kosco-Vilbois, K.M.Toellner, and M.Meyer-Hermann. 2008. Deriving a germinal center lymphocyte migration model from two-photon data. *J Exp Med* 205:3019-3029.
12. Filipe-Santos, O., P.Pescher, B.Breart, C.Lippuner, T.Aebischer, N.Glaichenhaus, G.F.Spath, and P.Bousso. 2009. A dynamic map of antigen recognition by CD4 T cells at the site of Leishmania major infection. *Cell Host Microbe* 6:23-33.
13. Germain, R.N., E.A.Robey, and M.D.Cahalan. 2012. A decade of imaging cellular motility and interaction dynamics in the immune system. *Science* 336:1676-1681.
14. Halford, W.P., J.W.Balliet, and B.M.Gebhardt. 2004. Re-evaluating natural resistance to herpes simplex virus type 1. *J Virol* 78:10086-10095.
15. Harris, T.H., E.J.Banigan, D.A.Christian, C.Konradt, E.D.Tait Wojno, K.Norose, E.H.Wilson, B.John, W.Weninger, A.D.Luster, A.J.Liu, and C.A.Hunter. 2012. Generalized Levy walks and the role of chemokines in migration of effector CD8+ T cells. *Nature* 486:545-548.
16. Heath, W.R. and F.R.Carbone. 2009. Dendritic cell subsets in primary and secondary T cell responses at body surfaces. *Nat Immunol* 10:1237-1244.
17. Hugues, S., A.Scholer, A.Boissonnas, A.Nussbaum, C.Combadiere, S.Amigorena, and L.Fetler. 2007. Dynamic imaging of chemokine-dependent CD8+ T cell help for CD8+ T cell responses. *Nat Immunol* 8:921-930.

18. Koya, R.C., S.Mok, B.Comin-Anduix, T.Chodon, C.G.Radu, M.I.Nishimura, O.N.Witte, and A.Ribas. 2010. Kinetic phases of distribution and tumor targeting by T cell receptor engineered lymphocytes inducing robust antitumor responses. *Proc Natl Acad Sci U S A*.

19. Lammermann, T., P.V.Afonso, B.R.Angermann, J.M.Wang, W.Kastenmuller, C.A.Parent, and R.N.Germain. 2013. Neutrophil swarms require LTB4 and integrins at sites of cell death in vivo. *Nature*.

20. McDonald, B., K.Pittman, G.B.Menezes, S.A.Hirota, I.Slaba, C.C.Waterhouse, P.L.Beck, D.A.Muruve, and P.Kubes. 2010. Intravascular danger signals guide neutrophils to sites of sterile inflammation. *Science* 330:362-366.

21. Mrass, P., H.Takano, L.G.Ng, S.Daxini, M.O.Lasaro, A.Iparraguirre, L.L.Cavanagh, U.H.von Andrian, H.C.Ertl, P.G.Haydon, and W.Weninger. 2006. Random migration precedes stable target cell interactions of tumor-infiltrating T cells. *J Exp Med* 203:2749-2761.

22. Mueller, S.N., W.Heath, J.D.McLain, F.R.Carbone, and C.M.Jones. 2002. Characterization of two TCR transgenic mouse lines specific for herpes simplex virus. *Immunol Cell Biol* 80:156-163.

23. Okada, T., M.J.Miller, I.Parker, M.F.Krummel, M.Neighbors, S.B.Hartley, A.O'Garra, M.D.Cahalan, and J.G.Cyster. 2005. Antigen-engaged B cells undergo chemotaxis toward the T zone and form motile conjugates with helper T cells. *PLoS Biol* 3:e150.

24. Peters, N.C., J.G.Egen, N.Secundino, A.Debrabant, N.Kimblin, S.Kamhawi, P.Lawyer, M.P.Fay, R.N.Germain, and D.Sacks. 2008. In vivo imaging reveals an essential role for neutrophils in leishmaniasis transmitted by sand flies. *Science* 321:970-974.

25. Rose, D.M., R.Alon, and M.H.Ginsberg. 2007. Integrin modulation and signaling in leukocyte adhesion and migration. *Immunol Rev* 218:126-134.

26. Schaeffer, M., S.J.Han, T.Chtanova, G.G.van Dooren, P.Herzmark, Y.Chen, B.Roysam, B.Striepen, and E.A.Robey. 2009. Dynamic imaging of T cell-parasite interactions in the brains of mice chronically infected with Toxoplasma gondii. *J Immunol* 182:6379-6393.

27. Semmling, V., V.Lukacs-Kornek, C.A.Thaiss, T.Quast, K.Hochheiser, U.Panzer, J.Rossjohn, P.Perlmutter, J.Cao, D.I.Godfrey, P.B.Savage, P.A.Knolle, W.Kolanus, I.Forster, and C.Kurts. 2010. Alternative cross-priming through CCL17-CCR4-mediated attraction of CTLs toward NKT cell-licensed DCs. *Nat Immunol* 11:313-320.

28. Toebes, M., M.Coccoris, A.Bins, B.Rodenko, R.Gomez, N.J.Nieuwkoop, W.van de Kasteele, G.F.Rimmelzwaan, J.B.Haanen, H.Ovaa, and T.N.Schumacher. 2006. Design and use of conditional MHC class I ligands. *Nat Med* 12:246-251.

29. Vroomans, R.M., A.F.Maree, R.J.de Boer, and J.B.Beltman. 2012. Chemotactic migration of T cells towards dendritic cells promotes the detection of rare antigens. *PLoS Comput Biol* 8:e1002763.

30. Weeks, B.S., R.S.Ramchandran, J.J.Hopkins, and H.M.Friedman. 2000. Herpes simplex virus type-1 and -2 pathogenesis is restricted by the epidermal basement membrane. *Arch Virol* 145:385-396.

31. Wilson, E.H., T.H.Harris, P.Mrass, B.John, E.D.Tait, G.F.Wu, M.Pepper, E.J.Wherry, F.Dzierzinski, D.Roos, P.G.Haydon, T.M.Laufer, W.Weninger, and C.A.Hunter. 2009. Behavior of parasite-specific effector CD8+ T cells in the brain and visualization of a kinesis-associated system of reticular fibers. *Immunity* 30:300-311.

SUPPLEMENTARY TEXT

Influence of infection size on attraction and spatial distribution of effector T cells

The analysis of cell migration demonstrates an attraction towards the foci of infection of antigen-specific and 'bystander' effector T cells (Fig. 2E,F in main text). However, it is also apparent that the strength of attraction (the deviation in angles to infection from 90 degrees) varies between experiments. We considered the possibility that the size of HSV foci may affect the strength of the chemoattractant gradient, such that bigger foci of infection may attract CTLs more strongly. We therefore quantified the size of the infection at the beginning of each experiment and measured the strength of directed migration, by calculating the mean of angles to infection up to a distance of 200 µm. The relationship between these two measures shows that effector CD8$^+$ T cells are more strongly attracted towards big than towards small microlesions (Fig. S4A), although there appears to be a saturation effect for very big infections. Since microlesion size influences attraction strength (Fig. S4A), and attraction strength influences effector T cell arrival at microlesions, we predicted that for big foci of infection a larger fraction of CTLs should be located close to the microlesion than for small foci. We quantified the spatial distribution of effector T cells at the beginning of each experiment by calculating the median of their distances to the infection. As predicted, for large foci, CTLs were located at shorter median distances than small infections (Fig. S4B). These data indicate that the volume of the infected microlesion correlates with the strength of effector T cell attraction, and – presumably because of this – the spatial distribution of these cells around the lesion. Note that these data are also consistent with a scenario in which T cells arriving early at infection foci secrete chemokines upon target encounter, thereby reinforcing the attraction of yet more effector T cells (in a similar fashion, specific CD8$^+$ T cells clustering around malaria-infected hepatocytes were proposed to locally secrete factors that result in the recruitment of additional effector T cells; Cockburn et al., 2013).

Because the size of the infection affects the behavior of surrounding T cells, in the analyses presented in the main text, only infections with a minimum volume of 50,000 µm^3 (as estimated from the image voxels assigned to infected cells) were included. Note that small infections below this threshold were primarily observed for HSV$_{\text{TOM-OVA}}$, suggesting that this modified virus grows out less efficiently than HSV$_{\text{TOM}}$.

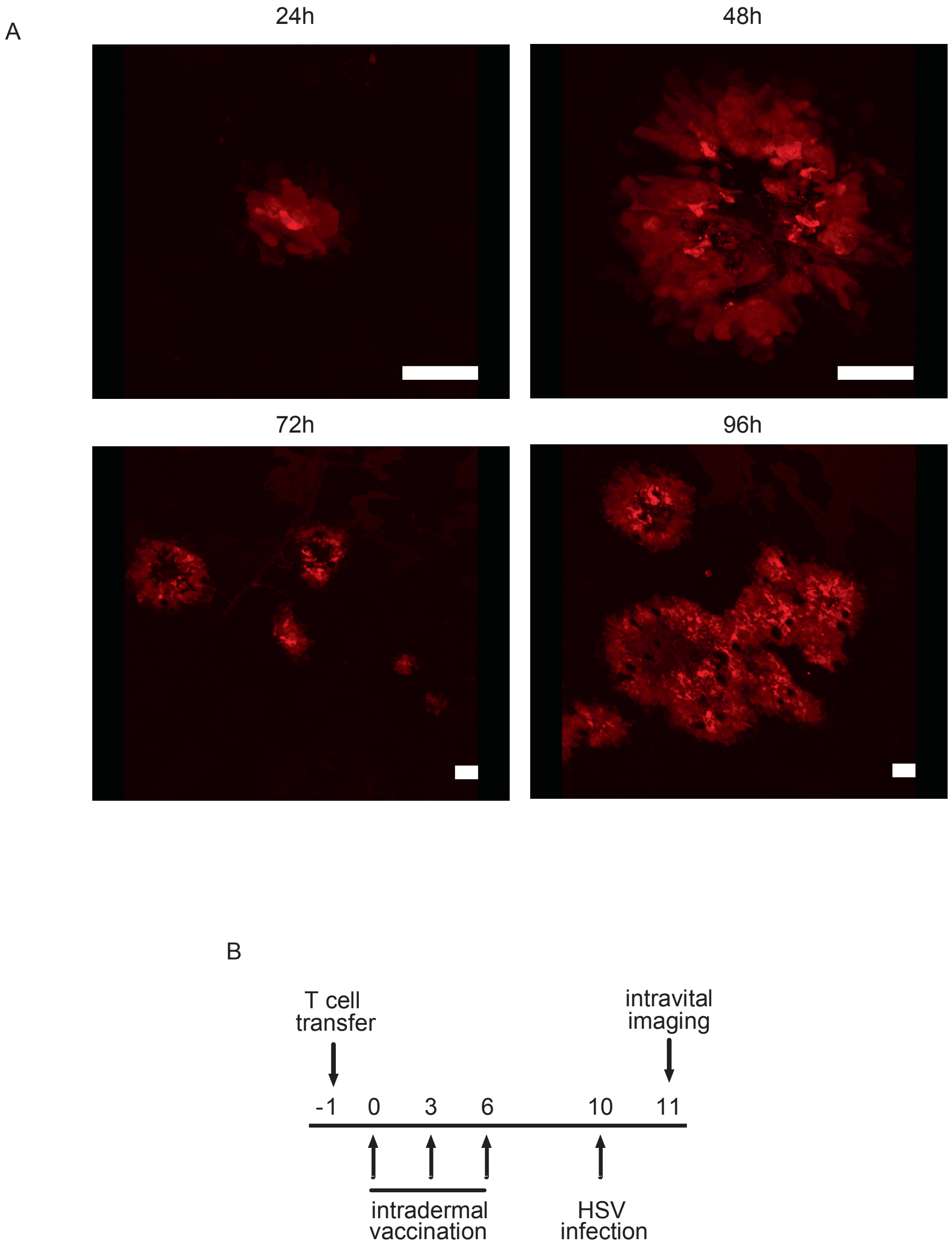

Figure S1. Model for visualizing T cell responses in HSV-1 infection.
(A) Confocal images of HSV$_{TOM}$ infected area (red) at different time points after infection with HSV$_{TOM}$. Bars = 100µm. **(B)** Schematic representation of the experimental setup.

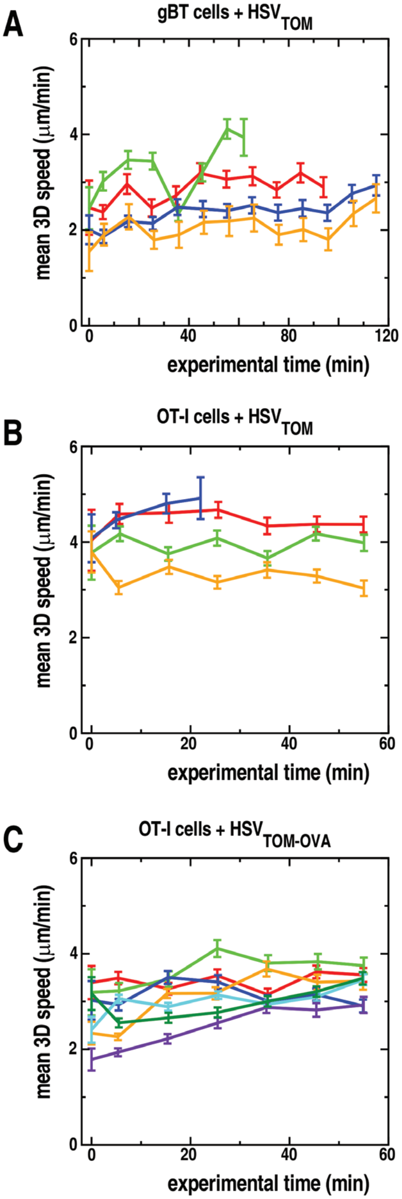

Figure S2. T cell speed is not influenced by imaging.
The mean 3D speed of T cells present within the imaged area is plotted over the time course of each experiment. Speed data were divided in bins of 10 minutes, and for each bin the mean speed versus the mean time in the bin is plotted (error bars show standard error of the mean). Results are shown for gBT (4 videos from 4 mice; panel A) and OTI T cells in animals infected with HSV$_{TOM}$ (4 videos from 4 mice; panel B), and for OTI T cells in animals infected with HSV$_{TOM-OVA}$ (7 videos from 7 mice; panel C). Colored bars represent individual videos. Note that the overall speed of antigen-specific T cells is lower than that of bystander T cells, due to ag-specific arrest of T cells close to the infection (see Figure 2C in main text).

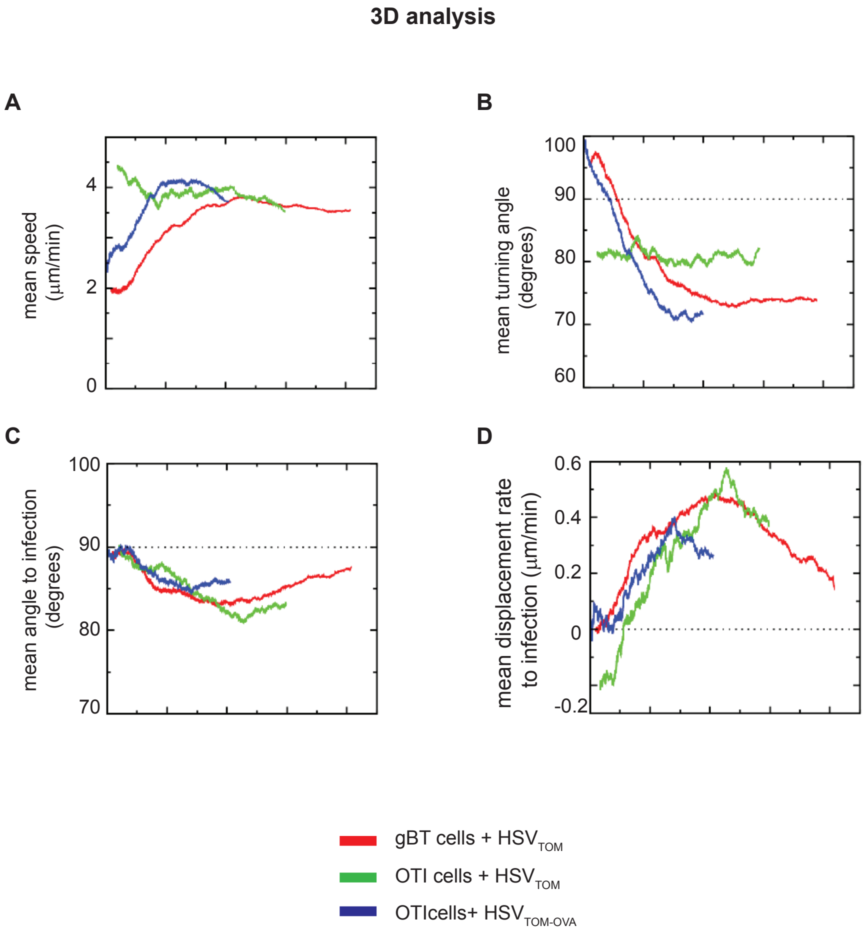

Figure S3. 3D analysis of cell migration.
(A-D) The mean speed (A), mean turning angle (B), mean angle to infection (C) and displacement rate towards infection (D) are depicted as a function of distance from infection in a 3D analysis. All tracked movement steps were sorted according to distance from infection (after merging data from multiple experiments), and a running average of 2,000 data points was plotted. Shown is the behavior of GFP-gBT T cells (4 videos from 4 mice; red) and GFP-OTI T cells in animals infected with HSV$_{\text{TOM}}$ (4 videos from 4 mice; green) and of GFP-OT-I T cells in animals infected with HSV$_{\text{TOM-OVA}}$ (3 videos from 3 mice; blue). The corresponding 2D analysis is shown in Fig. 2 in the main text.

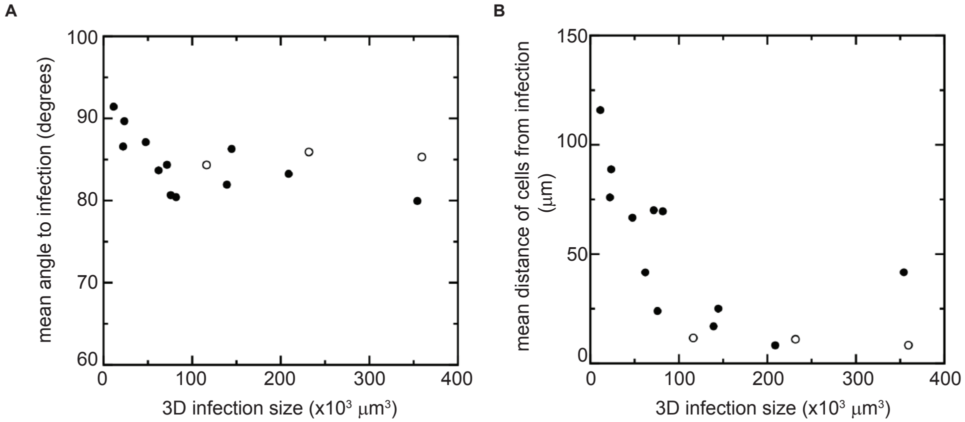

Figure S4. Correlation of HSV-1 infected microlesion size and T cell attraction and spatial distribution. (A and B). Attraction strength (A) and spatial distribution (B) of effector T cells are plotted as a function of the measured 3D microlesion size at the start of each experiment (data from 17 imaging regions in total). To allow for a fair comparison between experiments, distance data above 200 µm from infection were discarded for all experiments (open circles indicate videos for which the most remote data point was less than 200 µm from infection, and closed circles indicate experiments for which the most remote data point was at least 200 µm from infection). As a measure of attraction strength, we first calculated the mean 2D angle to infection per distance-to-infection bin of size 20 µm, and subsequently calculated the mean of all 10 bins (from 0 µm to 200 µm distance from infection) for each video. This was done to prevent that the large inter-experimental variation in the fraction of data points close to and far away from the infection would affect the results (for example, a strong chemoattraction by a lesion could be obscured by the fact that many cells already arrived at the infection, due to the very same attraction). As a measure of spatial distribution of cells, the median distance from infection of all cells present at the first time point of imaging (i.e., at 24 hours post infection) was calculated.

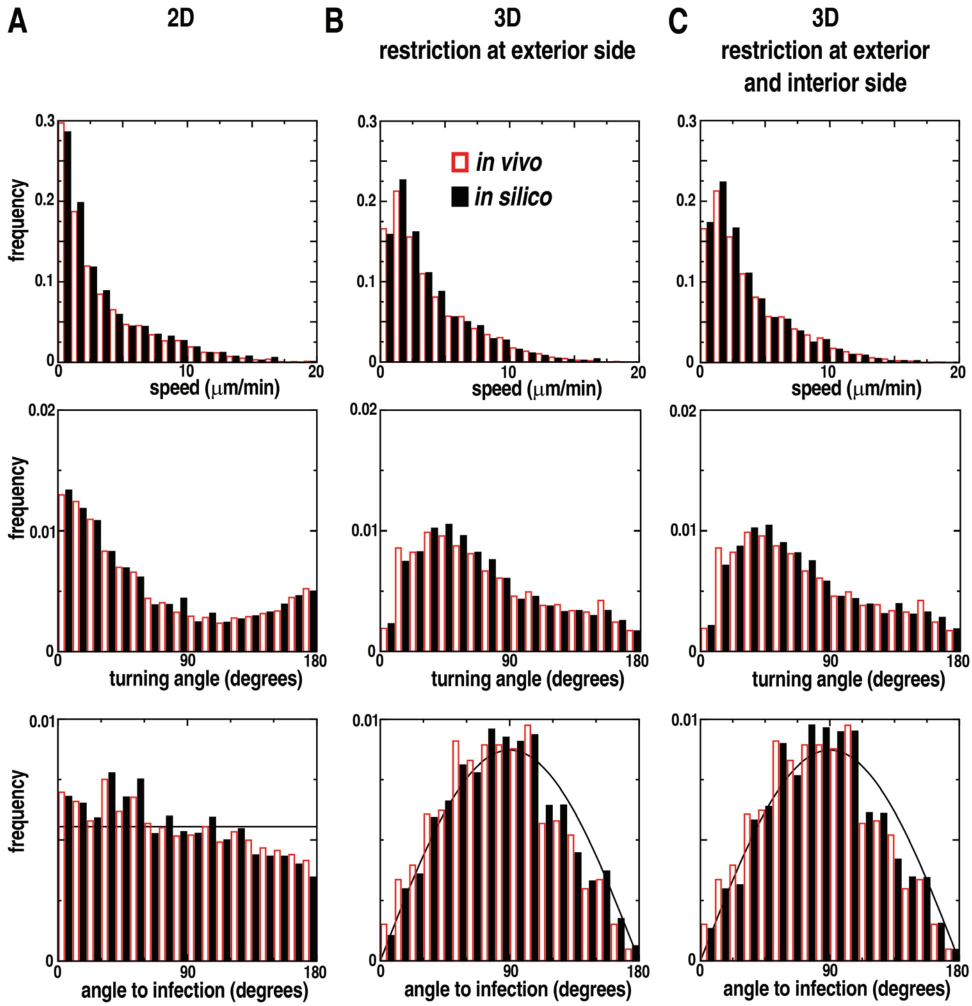

Figure S5. Simulations describe *in vivo* speed and angle distributions well.
(A-C) Frequency distributions (with the surface of the bars summing up to 1) of speeds (upper panels), turning angles (middle panels) and angles to infection (lower panels) are plotted for simulations of gBT T cells, as well as for experimental gBT T cell migration data. *In silico* data are generated by having cells start at a 150 μm distance from an infection with radius $r = 100$ μm and simulating until they reach a 50 μm distance, or leave the simulated space. For the *in vivo* data all movement steps occurring at distances to infection of 50-200 μm are used. Results are shown for 2D simulations (A), 3D simulations with restriction at the exterior side (B) and 3D simulations with restriction at both the exterior and interior side (C). The black line in the lower panels gives the distributions expected for random migration (note that these expectations depend on the dimensionality of the space (Beltman et al., 2009). Together, all panels show that there is good correspondence between the *in vivo* and *in silico* distributions of speeds and migration angles.

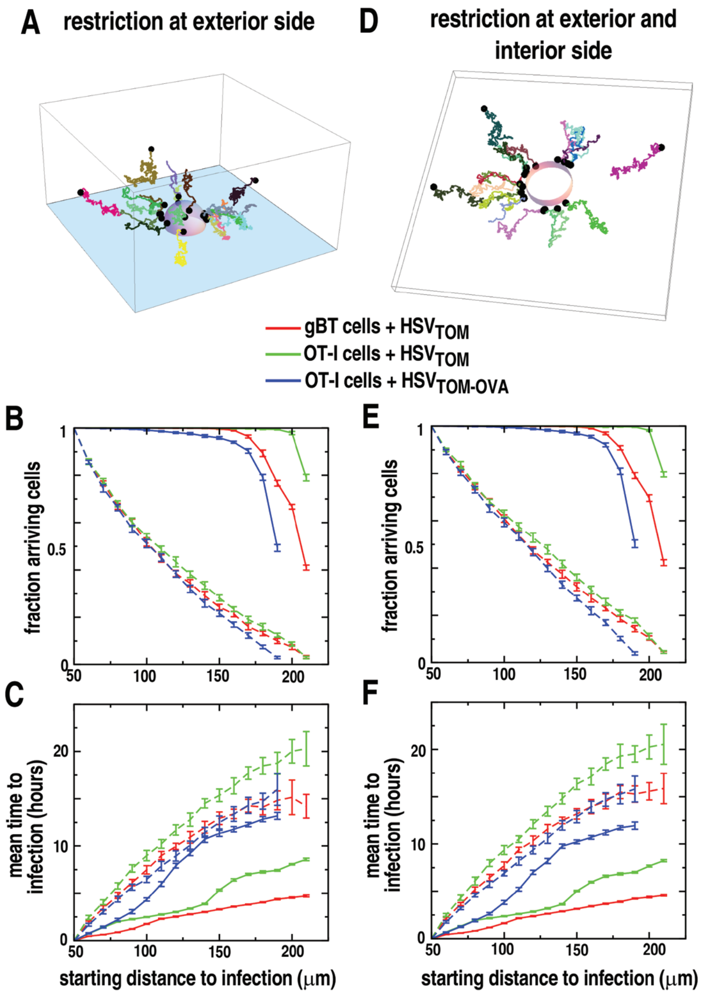

Figure S6. 3D simulations demonstrate effective and fast arrival of effector T cells at target site. **(A and D)** Example of tracks of 20 *in silico* gBT T cells starting at a 150 μm distance from an infection with radius *r*=100 μm, constructed by 3D simulations with restriction at the exterior side (A), or at both the exterior and interior side (D). The purple-colored hemi-sphere/ring represents the simulated infection, dots represent the final position of the simulated cells. **(B, C and E, F)** The fraction of cells arriving at a 50 μm distance from an infection with radius *r*=100 μm (B, E) and the mean time to achieve that position (C, F), when starting from various distances from the infection in 3D simulations. For each starting distance from infection, 20 simulations of 1,000 cells were performed, and mean and standard deviations of the simulations are plotted. Results from directed simulations are depicted by solid lines, results from random simulations are depicted by dashed lines. Simulations are based on cell migration data from GFP-gBT T cells (red) and GFP-OTI T cells in animals infected with HSV_{TOM}, (green), and from GFP-OTI T cells in animals infected with $HSV_{TOM\text{-}OVA}$ (blue). Migration data from gBT T cells at distances to infection higher than about 210 μm were discarded in order to allow for a fair comparison between experimental conditions. The results of the 3D simulations are in accordance with those of the 2D simulations (Fig. 3 in main text), and demonstrate that the measured directional preference has a major effect on the kinetics and effectiveness of T cell arrival close to the infection.

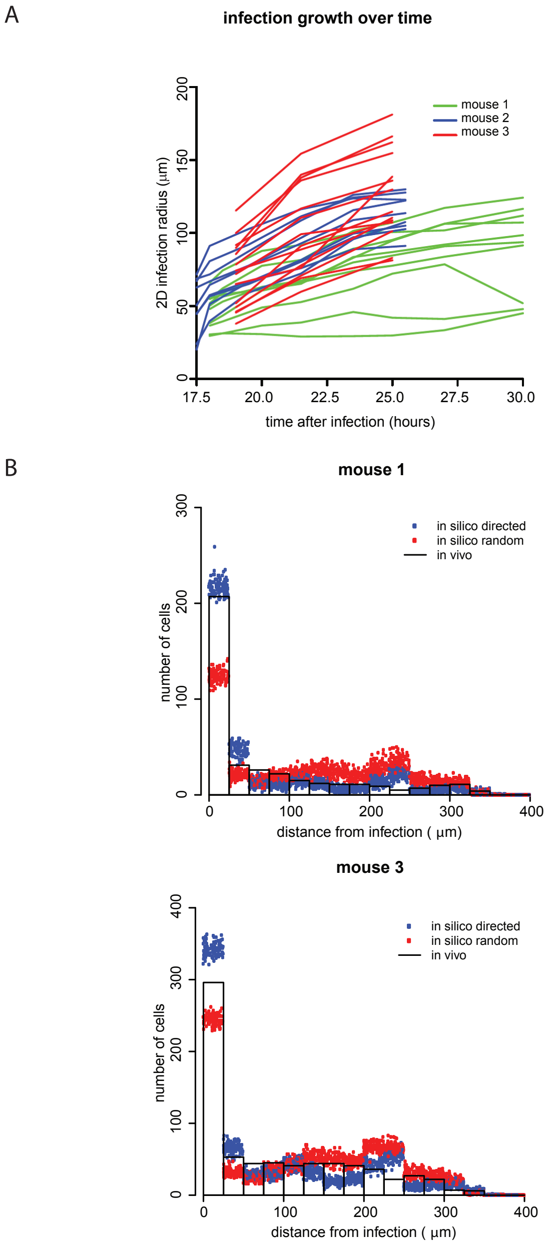

Figure S7. CTLs accumulate around infected microlesions over time.
(A) Evolution of infection growth over time for 31 different foci of three mice. Note that while our estimate of infection size is probably a slight underestimate, because fluorescence signal needs to build up to a sufficient level to allow detection, this is expected to be a constant effect and thereby unlikely to affect the estimate of the radial growth. **(B)** Comparison of the experimental spatial distributions of gBT cells and the distributions of gBT cells from 2D simulations in which migration was either directed or random, in the context of a growing infection. Results for two mice are shown; results for a third mouse as well as detailed explanation are shown in Figure 4 in the main text.

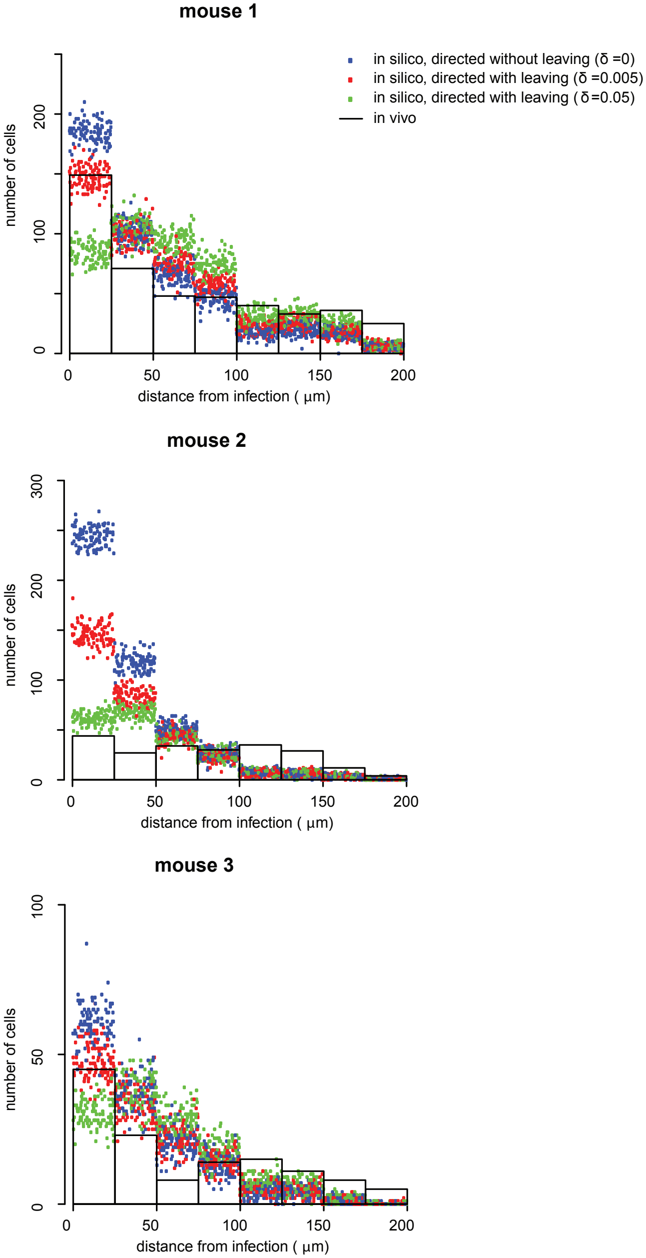

Figure S8. Directed migration alone cannot explain the accumulation pattern of bystander CTLs around infected microlesions over time.

Comparison of the experimental spatial distributions of OTI cells surrounding a HSV_{TOM} microlesion (based on 17 imaging regions from 3 mice) and the distributions of OTI cells from 2D simulations in which migration was either 'directed without leaving', or 'directed with leaving', in the context of a growing infection. In directed simulations with leaving, T cells that had reached the infection earlier during the simulation, left with probability δ at each time step.

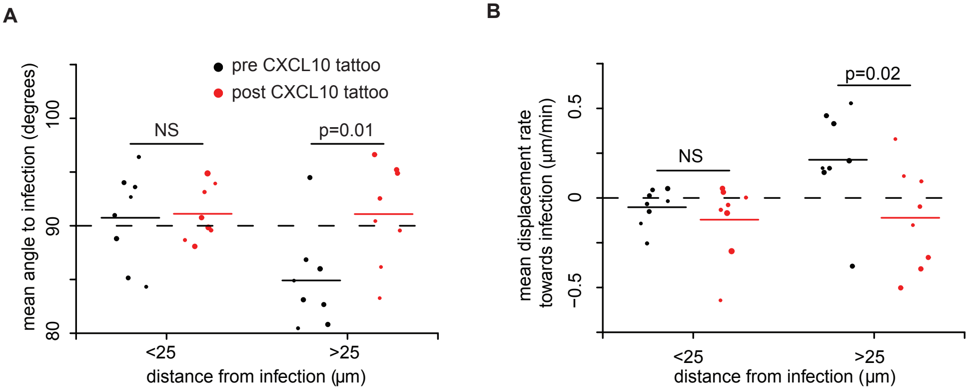

Figure S9. Directed migration of effector T cells is lost upon disturbance of chemokine gradient. **(A, B)** OTI T cells migrating towards an infected microlesion were imaged prior to or post local CXCL10 microinjection (to disrupt the chemotactic gradient). Movement steps were binned according to their distance to the infection, and the mean angle to infection (A) and mean displacement rate towards infection (B) of all steps within the bin was calculated (i.e., each infection focus is represented by two dots, one in each distance bin). The size of each dot is representative of the number of movement steps the average is based on, using a 'relative' log scale (e.g., a doubling of the radius of a circle implies a 10-fold increase in the number of data points). The 'post CXCL10 tattoo' analysis is based on 8 infection foci from three mice, and the 'pre CXCL10 tattoo' on 8 foci from 7 mice (combining the 5 foci from main text Fig. 2 with 3 newly imaged foci).

Video S1-S4. Representative videos of GFP-gBT (S1) and GFP-OT-I (S2, S3) T cells infiltrating areas infected with HSV$_{\text{TOM}}$ (S1, S2) or HSV$_{\text{TOM-OVA}}$ (S3). Bar = 50µm. **(S4)** Representative result of software-aided tracking analysis. Color represents the time index. Bar = 20µm; display rate 10 frames/second.

REFERENCES

1. Beltman, J.B., A.F.Maree, and R.J.de Boer. 2009. Analysing immune cell migration. *Nat Rev Immunol* 9:789-798.
2. Cockburn, I.A., R.Amino, R.K.Kelemen, S.C.Kuo, S.W.Tse, A.Radtke, L.Mac-Daniel, V.V.Ganusov, F.Zavala, and R.Menard. 2013. In vivo imaging of CD8+ T cell-mediated elimination of malaria liver stages. *Proc Natl Acad Sci U S A* 110:9090-9095.